

How to Evaluate and Manipulate Charge Transfer and Photocatalytic Response at Hybrid Nanocarbon–Metal Oxide Interfaces

Nina Kemnade, Paul Gebhardt, Greta M. Haselmann, Alexey Cherevan, Gerhard Wilde, and Dominik Eder*

Nanocarbon–metal oxide hybrids are among the most promising functional materials in many cutting-edge environmental and energy applications where efficient charge separation and extraction are keys to success. The next level of hybrid structures will be achieved once one learns how to control and tune charge/energy transfer processes at the interfaces. However, little is yet known about the nature and extent of these interfacial dynamics in nanocarbon hybrids. Here a model is designed in which ultrathin dielectric layers (Al_2O_3 , ZrO_2) between the hybrid's components (ZnO , TiO_2) and carbon nanotubes allow for evaluating and tuning of interfacial charge transfer over an unusually long distance of at least 50 nm. Surprisingly, the transfer efficiency correlates linearly with the barrier layer thickness, indicating that electron conduction through the barrier layer constitutes the rate-limiting step. It is also demonstrated that the charge transfer efficiency can be tuned by the type of interlayer and its degree of crystallinity, thus controlling the hybrid's performance in the photocatalytic production of hydrogen. It is believed that this model system will help to understand and decipher the fundamentals regarding interfacial charge and energy transfer in nanocarbon hybrids with the aim to further advance these hybrid structures for a wide range of energy applications.

1. Introduction

Recent years have seen the introduction of a new generation of active materials for applications in socioeconomically important areas, such as energy (e.g., photovoltaics, photocatalysis, batteries, supercapacitors), environment and health (e.g., water

and air purification, biosensors), and information technology (e.g., field emission devices, circuit elements).^[1–3] All of these applications rely on efficient charge separation and extraction. One promising strategy involves the designing of multifunctional materials through rational hybridization of two complementary compounds, i.e., a nanocarbon (e.g., graphene, carbon nanotubes—CNTs) with an active inorganic nanomaterial (e.g., transition metals, metal oxides, metal nitrides, perovskites, zeolites, etc.). These new hybrids feature both, a ready gas and liquid access to a large internal active surface area as well as extended interfaces that greatly enhance charge separation and extraction.

The efficiency of these hybrids relies on the nature and extent of interfacial charge and energy transfer between the two components. These depend on the electronic properties of the individual components, i.e., band position and gap energy, charge carrier concentration and mobility,^[2,4] and are further governed by

the nature of interfaces (e.g., proximity, type of interaction/electronic junction, presence of a mediator, etc.).^[5] It is crucial to evaluate these characteristics in order to understand and potentially manipulate the nature and extent of interfacial processes.

So far, however, while there is a full body of research on interfacial charge transfer in organic–inorganic hybrid structures in general,^[6–11] there are far less experimental^[12–16] and theoretical^[17–19] works in the field of CNT hybrids. Moreover, the majority of research work has merely assumed the presence of charge transfer in such hybrids. Only few attempts have been made to experimentally evaluate these processes, e.g., with fluorescence quenching and pump–probe spectroscopy.^[20] These have focused on hybrids with molecular fluorophores or quantum dots and reported contradicting results, supporting either electron^[21–23] or energy transfer.^[24] There have been only very few studies on hybrids with transition metal oxides despite their preferential use in photocatalytic applications.^[25,26] For example, Kamat and co-workers have observed fluorescence quenching of ZnO in composites with increasing amounts of CNTs.^[27,28] Still, none of these works

Dr. N. Kemnade, Prof. D. Eder
Institute of Physical Chemistry
Westfälische Wilhelms-Universität
Corrensstrasse 28/30, 48149 Münster, Germany
E-mail: dominik.eder@tuwien.ac.at

Dr. P. Gebhardt, G. M. Haselmann, Dr. A. Cherevan, Prof. D. Eder
Institut für Materialchemie
Technische Universität Wien
Getreidemarkt 9/BC/2, 1060 Vienna, Austria

Prof. G. Wilde
Institute of Materials Physics
Westfälische Wilhelms-Universität
Wilhelm-Klemm-Str.10, 48149 Münster, Germany

DOI: 10.1002/adfm.201704730

have sufficiently distinguished between charge and energy transfer, investigated particle size effects and interparticle quenching, or considered potential contributions by the nanocarbon through light absorption and scattering. We want to emphasize the necessity of a well-controlled model system, if one truly wants to understand and decipher the fundamentals regarding interfacial charge and energy transfer in nanocarbon hybrids with the aim to further advance these hybrid structures for energy applications.

In this work, we present a model system that is capable of deconvolution of the various quenching contributions and also allows for tuning of interfacial processes. The concept of this model system is based on the assumption that the fluorescence of a metal oxide layer that is typically quenched in the proximity of a CNT will be gradually retained by the introduction of a dielectric barrier layer with increasing thickness (Figure 1A). We have thus designed a system, in which ultrathin layers of Al_2O_3 and ZrO_2 were incorporated between the hybrid's components, i.e., ZnO and CNTs, with atomically precise control of thickness varied between 2 and 100 nm.

A key characteristic of our model system is that all tested samples contain the same CNT concentration, which allows for eliminating the contribution of light absorption from the nanocarbon. The presence of an Al_2O_3 layer in all samples also functions as a growth substrate and further ensures the deposition of ZnO particles with uniform and comparable size, morphology, packing, and defect structure, thus eliminating intrinsic quenching contributions within ZnO. That leaves only charge and energy transfer, which can be deciphered through distance-dependent quenching studies using solid-state photoluminescence (PL) spectroscopy.

Beside the proof-of-concept of this model system, we further demonstrate that we can tailor the extent of charge transfer by varying the type, crystallinity, and thickness of the barrier layers, ultimately controlling the performance of a CNT- TiO_2 hybrid in the photocatalytic production of hydrogen from aqueous solutions. We believe that both model system and concept are extendable to many other functional hybrids and will help gaining deeper insight into various interfacial processes that are key to a wide range of energy applications.

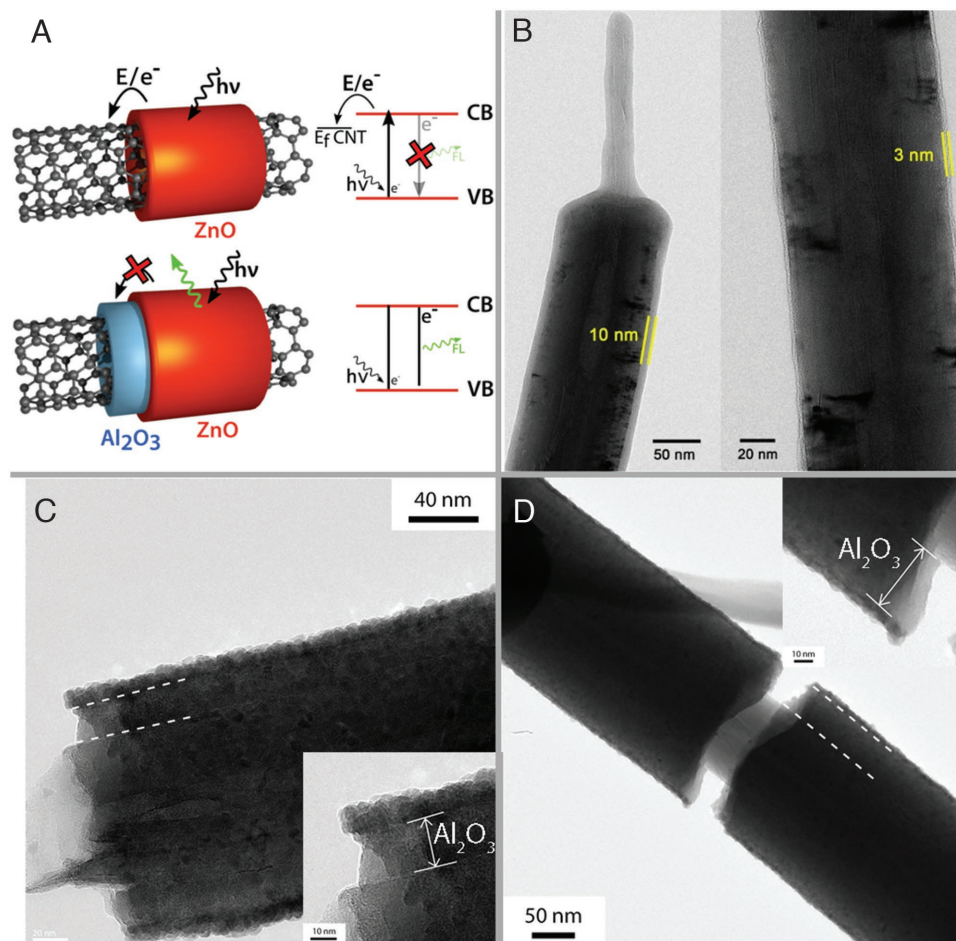


Figure 1. A) Schematic of our model system: direct hybridization causes fluorescence quenching due to interfacial charge/energy transfer (top), while a barrier layer causes distance-dependent suppression of charge/energy transfer (bottom). HRTEM images of different CNT hybrids showing B) the deposition of 3 and 10 nm thick Al_2O_3 layers on CNTs and the additional deposition of a 10 nm ZnO layer on top of CNT hybrids with C) 18 nm and D) 36 nm thick Al_2O_3 layers.

2. Results and Discussion

A major challenge in designing this model system was the need to deposit ultrathin, conformal coatings on highly porous CNT scaffolds with atomically controlled thickness and uniformity with unparalleled precision. We therefore employed atomic layer deposition (ALD), a highly versatile coating technique, predominantly used to process flat microelectronic devices. However, the complexity of the ALD process and the experimental setup along with the nature of the nanocarbon scaffold (i.e., high aspect ratio, tendency to form bundles, hydrophobicity) have so far limited wide-spread use of ALD for nanocarbon hybrid synthesis.^[29–32] Recently, we have developed an ALD process, in which a predeposited dense monolayer of pyrene carboxylic acid (PCA) with sufficiently strong van-der-Waals interactions with the carbon surface operated as an aromatic linker to allow coating of CNTs with metal oxides in a highly uniform, conformal, and—most importantly—non-destructive manner.^[33,34]

In this work, we utilized home-grown metallic multiwalled CNTs^[35] that were annealed in argon at high temperatures to remove carbonaceous material and residual iron catalyst and to improve the degree of graphitization (for more details, see Figures S1–S3, Supporting Information). The purified CNTs were then vacuum assembled into porous membranes with high porosity (Figure S4, Supporting Information) and subjected to an ethanol-assisted PCA vapor in an autoclave, which allowed for the deposition of a PCA monolayer onto the CNT surface.^[33] The PCA-modified membranes were then ALD coated with thin layers of metal oxides at 200 and 90 °C for Al₂O₃ and ZnO, respectively. Further experimental details, including the various ALD parameters, can be found in Supporting Information.

Figure 1B shows exemplary transmission electron microscopy (TEM) images of Al₂O₃-coated CNTs, which document that the individual CNTs within the entire membrane were homogeneously coated by Al₂O₃ layers with remarkably uniform thickness. The left image further shows the same coating on both large diameter CNT and thin CNT appendix, grown on the tip of the larger tube, which indicates that the curvature of the CNT does not affect the coating characteristics significantly. The film thickness correlated nicely in linear fashion with the number of ALD cycles (Figure S5, Supporting Information), which we varied from 10 to 600, corresponding to 2 to 105 nm, respectively. This was confirmed by comparative studies with atomic force microscopy (AFM) and ellipsometry (Figure S5, Supporting Information), which yielded a growth rate of 0.175 nm per cycle.

Figure 1C,D shows the TEM images of a thin capping layer of ZnO deposited on top of the Al₂O₃-CNT hybrids. Note that the ZnO nanoparticles are highly uniform in size and shape, which marks an important criterion for the spectroscopic studies in this work. The growth rate for ZnO was determined by AFM with 0.204 nm per cycle (Figure S6, Supporting Information) and yielded particle sizes of 5–20 nm for 25 to 100 cycles, respectively. It is important to note that the crystal size of ZnO deposited on PCA-modified CNTs without Al₂O₃ was slightly larger (e.g., 11.6 nm for 25 cycles, Figures S7 and S8, Supporting Information). Therefore, the presence of an Al₂O₃ layer as a substrate for ZnO growth is indeed crucial to ensure comparable

grain size. In all following samples, we fixed the thickness of the ZnO layer to 10 nm, which gave the optimized fluorescence behavior (Figure S15, Supporting Information).

The samples were investigated by X-ray diffraction (XRD), X-ray photoelectron spectroscopy (XPS), and electron microscopy high resolution transmission electron microscopy (HRTEM). In all samples, the ZnO particles were highly crystalline and of wurtzite structure (Figure S8, Supporting Information). Crucially, the ZnO crystals exhibited no noticeable grain boundaries in direction to the Al₂O₃-CNT surface (Figure S7, Supporting Information). This is in fact highly preferable for our investigations, since grain boundaries would induce additional charge transfer paths and quenching effects.^[36] Based on our XPS data (Figures S20 and S21, Supporting Information), we can also exclude the presence of metallic Zn, as well as the formation of Al-Zn alloys and the doping of ZnO with Al, which has occasionally been reported in literature.^[37]

We also designed two adequate reference materials to account for various quenching contributions: one, named “reference A”, which resembles the same morphology as the hybrids (i.e., crystal size, crystal packing, surface area, and porosity), yet does not contain CNTs; and a second, named “reference B”, which contains the same amounts of CNTs (i.e., to account for light absorption effects), yet exhibits no direct contact between the two components (i.e., to account for interfacial processes).

“Reference A”: Our first idea was to remove the CNTs from the Al₂O₃-ZnO hybrid through oxidation at elevated temperatures.^[38–40] However, the required oxidation temperature of 800 °C also led to a considerable growth of ZnO particles (Figure S9a,b, Supporting Information). Therefore, we calcined the respective Al₂O₃-CNT hybrids prior to the deposition of ZnO nanocrystals to remove the CNTs. During this treatment, the amorphous alumina coating unavoidably crystallized into γ -Al₂O₃ (Figure S10b, Supporting Information). These carbon-free Al₂O₃ tubes were subsequently decorated by ALD with ZnO crystals, which shared a comparable size and shape as our hybrid model systems (Figure S9c, Supporting Information).

“Reference B”: This sample was obtained by mechanically mixing “reference A” with corresponding amounts of CNTs. The purpose of this reference sample was to mimic the dimensions and concentration of the individual components of our model system, yet preventing close interfacial contact and hence charge transfer, thus accounting for absorption effects by the nanocarbon.

All samples were characterized by solid-state PL spectroscopy in total reflectance mode using an excitation wavelength of 325 nm. The use of freestanding membranes allowed for eliminating potential contributions from electronic interactions with solvents and substrates (Figures S11 and S12, Supporting Information). As expected, the uncoated CNT membranes showed no significant emissions in the measured range (Figure S13, Supporting Information). Figure 2A shows the PL spectrum of “reference A”, which consisted of two broad emission peaks centered at around 385 and 640 nm that can be assigned to direct fluorescence relaxation (DE) and defect-related deep-level emission (DLE), respectively.^[41,42] “Reference B” showed a similar emission spectrum, yet with 20% lower peak intensities than the CNT-free “reference A” (Figure 2A), which confirms that absorption effects by CNTs must not be neglected.

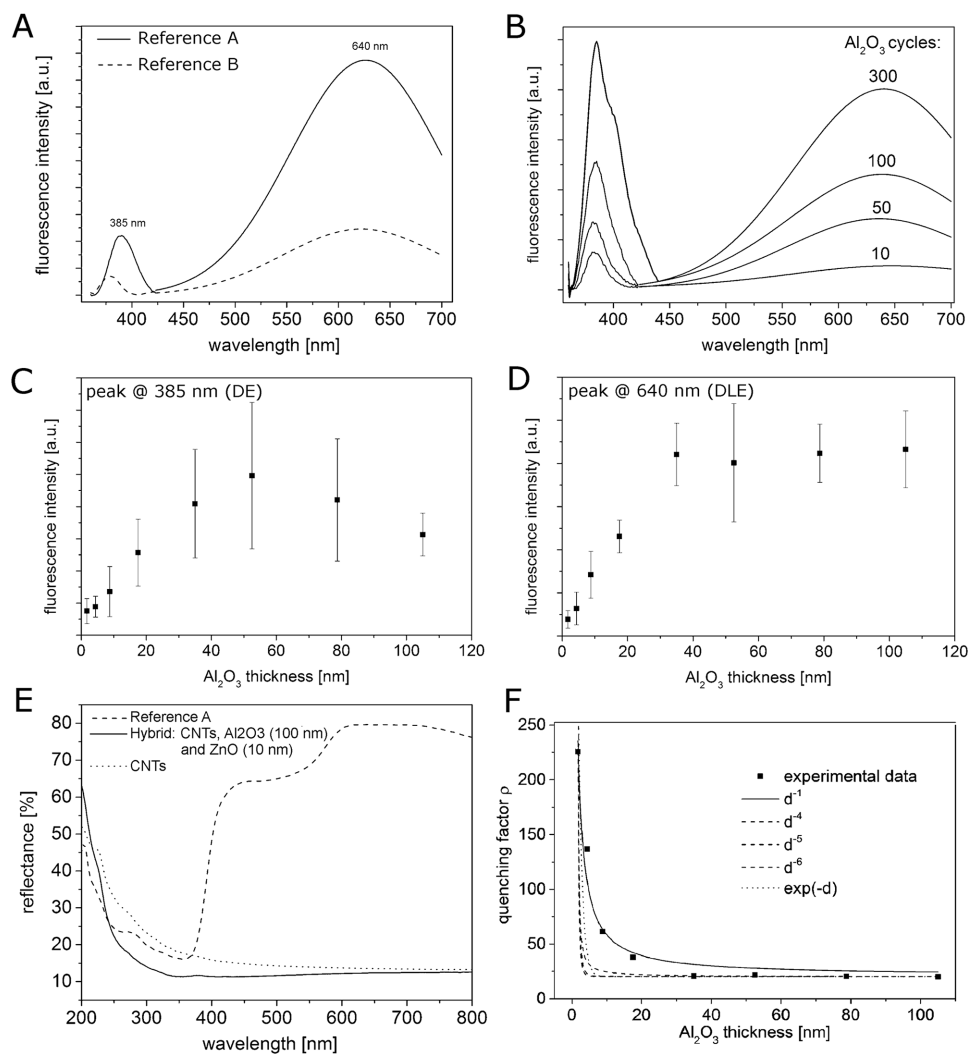


Figure 2. A) Fluorescence spectra of “reference A” (i.e., ZnO-coated Al_2O_3 tubes without CNTs) and “reference B” (i.e., mechanical mixture of ZnO-coated Al_2O_3 tubes and CNTs). B) Fluorescence spectra of ZnO/ Al_2O_3 /CNT hybrids with different Al_2O_3 thicknesses ranging from 2 to 60 nm, using an excitation wavelength λ_{Ex} of 325 nm. Correlation of fluorescence intensity with Al_2O_3 thickness for C) the DE peak and D) the DLE peak of ZnO, respectively, normalized to the respective intensities of “reference B” shown in (A). E) Diffuse reflectance spectra of pure CNTs, a hybrid of ZnO (10 nm)/ Al_2O_3 (100 nm)/CNT and “reference A”. F) Correlation of quenching factor with Al_2O_3 thickness fitted with various distance dependence models.

However, in contrast to “reference A”, the DE peak also contains the typically negligible fluorescence response by the free CNTs (Figure S13a, Supporting Information), which becomes dominating here and explains the noticeable peak shift down to 350 nm. The PL spectra for the model hybrids are summarized in Figures 2B (with additional spectra in Figures S16 and S17, Supporting Information). As expected, the direct hybridization of ZnO with CNTs has resulted in near-complete quenching of both PL peaks (Figure S16, Supporting Information), while the presence of an Al_2O_3 interlayer has mitigated this effect to an extent that depended on the thickness of the alumina layer.

To analyze this quenching behavior in more detail, we produced and measured 12 samples of every model hybrid, each with different Al_2O_3 layer thickness, in back and front irradiation mode (amassing to a total of about 100 samples and 200 data points). Figure 2C,D plots the corresponding average

PL intensities of the DE and DLE peaks, respectively, after normalization with respect to “reference B”. From these correlations, we can immediately make two intriguing observations: 1) the PL response of the model hybrids is considerably quenched even up to distances beyond 50 nm, which is farther than any reported values in literature,^[43–45] and 2) the quenching efficiency follows an unprecedented linear distance dependence for Al_2O_3 thicknesses below 50 nm and levels off at greater distances.

Fluorescence quenching in hybrid/composite materials can originate from several processes, including (1) radiative relaxation of photoexcited electrons (i.e., represented by DE or DLE); (2) nonradiative relaxation in the form of heat; (3) interparticle quenching between ZnO nanoparticles; (4) nanoparticle–surface interactions (e.g., between ZnO and Al_2O_3); (5) electromagnetic coupling between CNTs and ZnO due to energy and electron transfer; and, finally, (6) light absorption by CNTs.

In addition, as shown above, the emission intensity also depends on the size and shape of the ZnO nanoparticles.

Due to the characteristics of our model samples (i.e., uniform ZnO particle size, shape and packing, and alumina substrate), many of these contributions: nanoparticle–surface interactions, interparticle quenching, and radiative and nonradiative relaxations, can be either taken as constant or considered negligible. We further assume that the constant CNT content of the samples and the correlation with “reference B” account for light absorption effects and simple charge injection into the Al₂O₃ layer. However, to test whether the extent of light absorption by CNTs is affected by the different alumina layers, we investigated the samples with diffuse reflectance spectroscopy (DRS). Figure 2E shows the typical reflectance profiles for the CNT-free “reference A” and a hybrid with 100 nm Al₂O₃ layer thickness. Considering that both samples exhibit comparable morphology and dimensions, we can safely deduce from these data that the CNTs in the hybrids indeed absorbed light in the visible regime as efficiently as pure CNTs. This confirms that even the thickest alumina layers in our experiments did not diminish the absorption capacity of CNTs. Consequently, electromagnetic coupling between ZnO and CNTs remains the only plausible source for the observed quenching in our hybrid samples, and distance-dependent quenching studies should allow for distinguishing between interfacial energy and charge transfer.

A closer look at the PL spectra reveals that the intensity of both DLE and DE peak correlates linearly with alumina thickness up to about 60 nm, yet with a marked difference in magnitude. The quenching of the DLE peak is particularly strong, yielding a maximum intensity of only 17% versus “reference B” at around 35 nm. In contrast, the intensity of the DE peak reaches a maximum of 53% at 55 nm. This difference can be explained by correlating the fluorescence intensity with the lifetime of the excited states, which, in first approximation, affects the efficiency of charge and energy transfer. Literature values suggest three main pathways for charge relaxations in ZnO^[46]: (1) direct recombination of electrons and holes (i.e., DE) with lifetimes of about 12 ps, (2) nonradiative trapping of charge carriers near defect sites with shorter lifetimes of about 1 ps, and (3) the relaxation from defect sites to deeply trapped holes (i.e., DLE) with comparatively long lifetimes of 400 ps. Considering that a longer lifetime also increases the probability of electromagnetic coupling with the CNTs, it is understandable why the intensity of the comparatively slow DLE is reduced more efficiently than of the fast DE. Beyond 60 nm, the trend diverges from a linear dependence due to scattering contributions owing to the changing geometry of the hybrids (further discussion in Supporting Information).

To distinguish between charge and energy transfer, we calculated a quenching factor $\rho = \frac{I_0}{I}$ (see Supporting Information and ref. [24]), which is plotted with respect to the alumina layer thickness in Figure 2F for the DLE peak (for the DE peak, see Figure S17, Supporting Information). The experimental data are fitted with various known distance dependences for charge and energy transfer. For example, classical charge transfer decays exponentially, while energy transfer typically follows a distance dependence of d^{-6} .^[24,47] Recently, Swathi and Sebastian calculated diverging distance dependences of d^{-4} and d^{-5}

for fluorescence resonance energy transfer from a dye to a graphene sheet and a long semiconductor tube, respectively.^[48] Furthermore, charge transfer is commonly limited to about 2–3 nm, while energy transfer can proceed over distances from 1 to beyond 20 nm.

Interestingly, none of these classical models can satisfactorily explain the observed linear decay rate ($\approx d^{-1}$), nor can they account for the comparatively long quenching distance of our measurements. There is, however, an alternative explanation: linear distance dependence can arise when the electron transport through the alumina layer becomes the rate-limiting process. This hypothesis appears implausible at first, if one thinks of Al₂O₃ as a dielectric insulator. However, a closer look with HRTEM and electron diffraction (ED) reveals that the Al₂O₃ layers deposited at 200 and 300 °C were all amorphous (Figure 3). This is, in fact, in line with other reports on ALD.^[49] It is well known that amorphous oxides can provide defect-related diffusion paths^[50] and thus higher conductivities than their crystalline counterparts.^[51,52] Additionally, while crystalline Al₂O₃ is considered an insulator with a large bandgap, amorphous alumina enjoys a continuous distribution of sparsely occupied interband states and therefore a “quasi metallic behavior”^[53] that can potentially facilitate charge diffusion between ZnO and CNTs.

To confirm this hypothesis, we modified the barrier layer. In a first set of experiments, we decreased the reaction temperature for ALD from 200 to 90 °C that yielded crystalline Al₂O₃ coatings. The HRTEM and ED images in Figure 3B confirm that the Al₂O₃ films are polycrystalline and consist of nanoparticles of about 20–30 nm in size (Figure 3B). Due to the complexity of the model system, it was not possible to directly measure the conductivity of these ultrathin-conformal alumina layers. However, through comparison with literature, we can assume a lower conductivity of the polycrystalline film versus the amorphous films.^[51–53] Furthermore, it is important to note that we did not detect any significant changes in size, shape, or crystallinity of ZnO nanoparticles grown on either amorphous or crystalline Al₂O₃ films. PL studies on the samples with polycrystalline Al₂O₃ layers indeed revealed a similar linear quenching behavior, yet with stronger thickness dependence, as expected from the lower conductivity of the barrier layer (Figure 3C, the respected spectra are in Figure S18, Supporting Information).

In another set of experiments, we synthesized a series of model hybrids, where we replaced Al₂O₃ with ZrO₂ (Figure S19, Supporting Information). ZrO₂ exhibits a twice as high dielectric constant as Al₂O₃ and is thus expected to induce a stronger quenching behavior.^[36,41] Indeed, we again observed linear distance dependence, yet with a considerably steeper slope than with crystalline Al₂O₃ (Figure 4A). Interestingly, the implementation of a 2 nm thin Al₂O₃ layer in-between CNTs and the ZrO₂ layers did not affect the slope significantly, which further supports the hypothesis that the quenching process is predominantly guided by charge transport through the barrier layer rather than trapping at the interface.

These results confirm that the charge conduction through the barrier layer constitutes the rate-limiting process for the interfacial charge transfer. In order to understand the direction of charge transfer, we took a closer look into the electronic

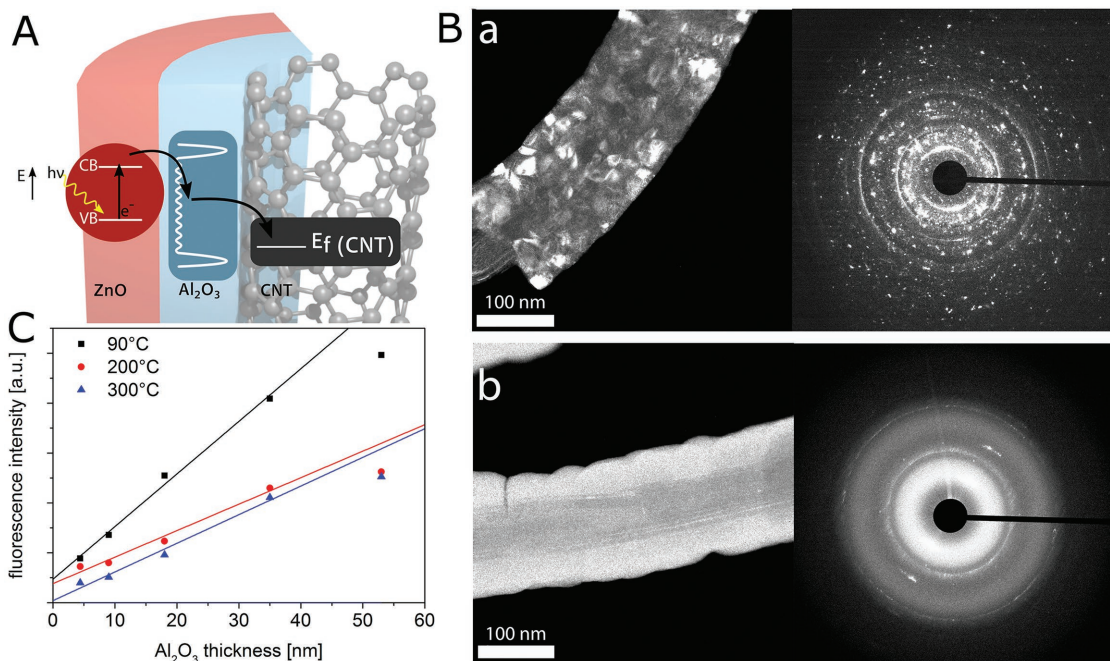


Figure 3. A) Schematic of the proposed charge transfer mechanism between ZnO and the CNT via inter-bandgap states within the barrier layer. B) TEM-DF images and corresponding electron diffractions of CNT hybrids with a 55 nm thick Al_2O_3 layer deposited at a) 90 and b) 300 °C, indicating a polycrystalline and amorphous nature, respectively. C) Correlation of fluorescence intensity with Al_2O_3 thickness for the DE peak of ZnO for different deposition temperatures of Al_2O_3 , suggesting an enhanced quenching behavior with the crystalline interlayer.

structure of the two hybrid's components.^[54–56] The potential energy of the conduction band of ZnO (i.e., electron affinity) lies at -4.2 – 4.3 eV.^[57,58] The Fermi level of CNTs depends on the type, defect concentration, and functionalization; hence, we have measured the work function of our metallic multiwalled carbon nanotubes (MWCNTs) (Figure S23, Supporting Information). The value of 4.8 eV is in line with literature data^[54] and confirms that the Fermi level lies well below the conduction band of ZnO. It is thus plausible to assume that photoexcited electrons will transfer toward MWCNTs rather than vice versa.

We thus propose a model based on the electronic coupling between ZnO and CNTs in three steps (Figure 3A): (a) the transfer of photoexcited electrons from ZnO to inter-bandgap

states of the barrier layer (i.e., Al_2O_3 or ZrO_2), (b) electron conduction through the barrier layer, and (c) interfacial charge transfer from the barrier layer to the CNT. The latter step is facilitated by the PCA molecules at the interface, which can act as a shuttle for electron injection into CNTs.^[55] The overall process is driven by a potential gradient induced between the photoexcited electrons in the conduction band of ZnO and the Fermi level of the CNTs. As the data show, the process can be tuned by modifying the thickness, the crystallinity (i.e., conduction pathways), and the type (i.e., dielectric constant) of the barrier layer.

Finally, to corroborate our charge transfer model, we tested our model hybrids for photocatalytic hydrogen evolution.

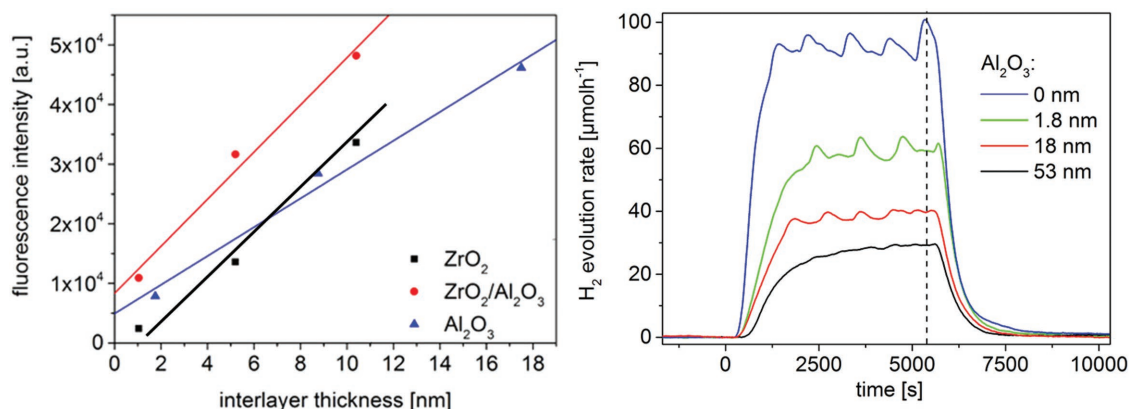


Figure 4. A) Distance-dependence of fluorescence intensities for hybrids with ZrO_2 (black line), $ZrO_2@2\text{ nm } Al_2O_3$ (red line), and Al_2O_3 (blue line) barrier layers: the steeper slope for both ZrO_2 layers indicates a stronger quenching behavior. B) Typical transient profiles of photocatalytic hydrogen evolution rates over TiO_2 - Al_2O_3 -CNT hybrids with different barrier layer thickness: the activity can be gradually tuned by the interlayer thickness.

This, however, required replacing ZnO with the photocatalytically more active TiO₂, while preserving both morphology and structure of the CNT–Al₂O₃ part (see experimental part). The photocatalytic membranes were immersed in water–methanol solution and illuminated with UV light using top illumination setup. No stirring or sonication was used in order to avoid peeling of the coatings. A CNT–TiO₂ hybrid without the barrier layer was used as a reference material: it showed the highest photocatalytic activity of about 90 μmol h⁻¹ (Figure 4B). Upon introduction of the barrier layer, we observed that the activity gradually decreased with increasing alumina thickness, eventually reaching a saturation level of about 25 μmol h⁻¹ for Al₂O₃ layers beyond 20 nm. These studies confirm that the photocatalytic activity is determined by the interfacial charge transfer, which supports our proposed charge transfer model. To the best of our knowledge, it also represents the first report that demonstrates how the photocatalytic performance of a CNT hybrid can be by tailored by means of interfacial engineering.

3. Conclusion

We have designed a unique model system that allows for in-depth investigation and tuning of interfacial charge transfer in nanocarbon–inorganic hybrids. The novelty originates from the introduction of ultrathin dielectric barrier layers of Al₂O₃ and ZrO₂ between a central CNT core and a decorating layer of ZnO nanoparticles. The barrier layers were deposited by a modified ALD process with atomically precise control of thickness varied between 2 and 100 nm that allowed for distance-dependent fluorescence quenching studies with solid-state PL spectroscopy. With this model system and the help of specially designed reference materials, we could eliminate all quenching contributions and identify an unusual electronic ZnO–CNT coupling behavior that was surprisingly far-reaching and prevailed even through alumina layers with a thickness beyond 50 nm, which is farther than any reported values in literature. We also observed that the quenching efficiency correlated with the thickness of the barrier layer in an unprecedented linear fashion. The efficiency could further be tuned by the type (e.g., ZrO₂) and the crystallinity (i.e., amorphous vs polycrystalline) of the barrier layer. Based on these findings, we discussed a quenching model, in which electron transport through the barrier layer constitutes the rate-limiting step. The tunability of this process was further tested for photocatalytic hydrogen evolution, where we demonstrated that the activity of the hybrid catalyst relies on an efficient electron transfer that can be tailored by the barrier layer. This work also demonstrates the importance of engineering interfaces in hybrid materials, which emerges as a powerful tool to next-generation functional materials in cutting-edge environmental and energy applications.

4. Experimental Section

CNT Synthesis: A floating catalyst chemical vapor deposition method (FCCVD) was used to produce MWCNTs according to ref. [26]. A solution of 4 wt% ferrocene in toluene was continuously injected into a two-stage horizontal tube furnace (type HZS, Carbolite, UK) at a rate of 5.4 mL h⁻¹ and carried in an argon flow (400 mL min⁻¹) into the reaction zone of

the quartz reaction chamber that was heated at 760 °C. After 90 min reaction time, the tube furnace was cooled to room temperature and the CNTs were collected.^[56] A typical batch contained CNTs with lengths between 100 and 200 μm and average outer diameter of ≈80 nm, as obtained by statistical analysis of about 60 bucky paper membranes. The specific surface area was determined by N₂ physisorption to be 47 m² g⁻¹ according to Brunauer–Emmett–Teller (BET).

Processing of CNTs: The as-grown CNTs were purified through annealing in argon at 2100 °C for 6 h to remove residual amorphous carbon and encapsulated iron catalyst residues and to anneal structural defects.^[1] The D:G ratio, which determines the graphitic quality of the CNTs and is obtained from Raman spectroscopy (Figure S2, Supporting Information), decreased from 0.32–0.39 for as-grown CNTs to 0.17 for the CNTs annealed at 2100 °C. Furthermore, thermal analysis (Figure S3, Supporting Information) showed that the remaining weight from residual Fe₂O₃ was reduced from 7.9% to 2.6%.

The CNTs were assembled into porous membranes (“bucky papers”, Figure S4, Supporting Information) to withstand the high vacuum conditions in the ALD chamber. Typically, 1.25 mg mL⁻¹ annealed CNTs were dispersed in ethanol, sonicated for 15 min and vacuum filtrated. Drying at room temperature yielded a mechanically stable “bucky paper” with a specific surface area of 25 m² g⁻¹ and a pore volume of ≈0.05 cm³ g⁻¹. The CNT membranes were then functionalized noncovalently with pyrene carboxylic acid (PCA–CNT) via a hydrothermal process. Typically, one mL of PCA in ethanol (1 mg mL⁻¹) was filled into a small Teflon beaker within a Teflon-lined autoclave (Parr Instrument Company, model 4749). The bucky paper was spatially separated to avoid pore collapse upon surface tension through liquid contact. The autoclave was heated at 215 °C for 2 h to prepare functionalized CNT membrane.

ALD: ZnO: The functionalized CNT bucky papers were placed inside the reaction chamber of a Savannah 100 ALD system (Cambridge Nanotech), which was purged with N₂ (20 sccm) for 5 min at a pressure to 0.2 Torr. For the ZnO deposition, the N₂ flow was reduced to 10 sccm before first water (oxygen source) and then the metal precursor (dimethyl zinc) were dosed into the reaction chamber with 0.03 and 0.05 s pulses, respectively. After each precursor injection, the CNT bucky papers were exposed to the reactant for 10 s before purging of the chamber with N₂ of 15 s. The reactor temperature was set to 90 °C and the injection cycle was repeated 50 times.

Al₂O₃: The deposition conditions differed only in the pulse duration of the metal precursor (trimethyl aluminum), which was reduced to 0.03 s, and increased exposure and purging times of 20 and 25 s, respectively. In addition, the cycle number was varied between 10 and 600 and the reactor temperature ranged from 90 to 300 °C to prepare crystalline and amorphous layers, respectively.

ZrO₂: Tetrakis(dimethylamido)zirconium—Zr(N(CH₃)₂)₄—was used as the precursor. The optimized parameters were 0.5 s as the pulse duration and 10 s as the exposure time, the purging times were 45–60 s, the deposition temperature was 250 °C. After deposition, the ZrO₂ layer was calcined at 400 °C, which was sufficiently low to avoid CNT oxidation.

TiO₂: The deposition procedure was similar to ZrO₂ due to the similar precursor of tetrakis(dimethylamido)titanium—Ti(N(CH₃)₂)₄. The deposition temperature, however, was 150 °C.

Characterization of Hybrids: The hybrids were characterized via SEM (Zeiss XB 1540 EsB) with an applied acceleration voltage of 2 kV and the use of a secondary electron detector. In addition, TEM (Zeiss Libra 200) with 200 kV electron beam acceleration voltage was used to obtain detailed information about morphology and crystallinity of the samples. Furthermore, the crystallinity of the deposited oxides was determined by XRD, using a Bruker D8 Advance instrument with Cu Kα irradiation and Bragg–Brentano geometry, which uses a beta filter (Ni) and a Lynxeye super speed detector. Raman spectra were measured via a Jobin Yvon Horiba LABRAM HR with a Nd:YAG-Laser (λ = 532 nm), charge coupled device (CCD), and optical microscope (Olympus BX41). N₂-Physisorption was performed with a Micromeritics ASAP 2010 at 77 K. The BET method was used to determine the total surface area, and the pore volume was calculated via Barret–Joyner–Halenda (BJH).

A TGA Q5000 (TA Instruments) was used for the thermogravimetric measurements. The samples were filled in an Al₂O₃-crucible and stabilized isothermally at 40 °C for 1 h. A temperature ramp from 30 to 1000 °C with 5 K min⁻¹ under N₂ was applied.

AFM was carried out on a Dimension 3100 (Digital Instruments) using tapping mode in air with a Tap300Al Silicon AFM probe. In addition to AFM, spectroscopic ellipsometry was used to measure the oxide thicknesses on silicon wafers. The ellipsometric measurements were performed with a Sentech SE 800 spectroscopic ellipsometer, with a wavelength range of 300–850 nm. The spectrum of each sample was recorded with two different incidence angles, i.e., 50° and 70°, and the obtained spectra were fitted with the two-phase optical model and the Cauchy model to get the thickness and refractive index of the coatings.

The optical properties of the coatings were further investigated via DRS using a Jasco V-670 UV-vis photo spectrometer. An Ulbricht sphere was used for light collection and the samples were measured with a 3 mm aperture. The fluorescence measurements (PL) were carried out in solid state mode with a Fluorolog 3-22 (Horiba Jobin Yvon) with a Xenon lamp as light source. For zinc oxide, 325 nm was used as excitation wavelength.

Photocatalytic Experiments: Photocatalytic sacrificial water splitting experiments were performed in a home-made top-illumination flow cell. Lumatec UV-vis light source equipped with a 200 W super pressure Hg lamp was used to provide UV irradiation necessary to photoexcite charge carriers in the TiO₂ capping layer through a quartz window by means of an optical fiber. Typically the reactor was filled with 5 mL H₂O and 5 mL methanol, and the photocatalyst bucky paper (TiO₂-Al₂O₃-CNT) was carefully immersed into the liquid. The solution was purged with Ar for 5 min to remove air bubbles attached to the bucky paper. A certain amount of the cocatalyst precursor (8 wt% aqueous H₂PtCl₆ solutions) was used for in situ Pt photodeposition. The used amounts were calculated to yield 2 wt% Pt with respect to the active TiO₂ photocatalyst mass. The reactor was closed and purged with Ar for another 15 min before illumination with light was started. Amounts of produced H₂ were monitored with an online gas analyzer (Emerson Process Management) equipped with thermal conductivity detector.^[6]

Supporting Information

Supporting Information is available from the Wiley Online Library or from the author.

Acknowledgements

This work was funded by the European Union's 7th Framework Program FP7/2007-2013 under grant agreement no. 310184 and by the Deutsche Forschungsgesellschaft (DFG ED 221/3-1). N.K. acknowledges financial support of the Graduate School of Chemistry at the University of Münster. The authors further thank Andreas Erbe (MPIE, Düsseldorf, Germany) for the ellipsometry measurements and the USTEM center at the TU Wien for support during electron microscopy studies.

Conflict of Interest

The authors declare no conflict of interest.

Keywords

atomic layer deposition, charge transfer, nanocarbon, nanocomposites, photocatalysis

Received: August 17, 2017

Revised: October 3, 2017

Published online:

- [1] D. Eder, *Chem. Rev.* **2010**, *110*, 1348.
- [2] C. J. Shearer, A. Cherevan, D. Eder, *Adv. Mater.* **2014**, *26*, 2295.
- [3] D. Eder, R. Schlögl, M. Antonietti, T. Bandosz, G. Centi, X. Feng, B. Frank, D. M. Guldi, Q. Li, M. Motta, K. Muellen, M. Prato, C. N. R. Rao, S. C. Smith, P. Strasser, D. S. Su, M. Terrones, J. J. Vilatela, *Nanocarbon-Inorganic Hybrids: Next Generation Composites for Sustainable Energy Applications*, De Gruyter, Berlin **2014**.
- [4] J. J. Vilatela, D. Eder, *ChemSusChem* **2012**, *5*, 456.
- [5] F. M. Wang, P. He, Y. Li, T. A. Shifa, Y. Deng, K. Liu, Q. Wang, F. Wang, Y. Wen, Z. Wang, X. Zhan, L. Sun, J. He, *Adv. Funct. Mater.* **2017**, *27*, 1605802.
- [6] D. A. Racke, L. L. Kelly, H. Kim, P. Schulz, A. Sigdel, J. J. Berry, S. Graham, D. Nordlund, O. L. A. Monti, *J. Phys. Chem. Lett.* **2015**, *6*, 1935.
- [7] S. Beck, D. Gerbert, T. Glaser, A. Pucci, *J. Phys. Chem. C* **2015**, *119*, 12545.
- [8] Y. Vaynzof, A. A. Bakulin, S. Gélinas, R. H. Friend, *Phys. Rev. Lett.* **2012**, *108*, 246605.
- [9] K. R. Siefertmann, C. D. Pemmaraju, S. Neppel, A. Shavorskiy, A. A. Cordones, J. Vura-Weis, D. S. Slaughter, F. P. Sturm, F. Weise, H. Bluhm, M. L. Strader, H. Cho, M.-F. Lin, C. Bacellar, C. Khurmi, J. Guo, G. Coslovich, J. S. Robinson, R. A. Kaindl, R. W. Schoenlein, A. Belkacem, D. M. Neumark, S. R. Leone, D. Nordlund, H. Ogasawara, O. Krupin, J. J. Turner, W. F. Schlotter, M. R. Holmes, M. Messerschmidt, M. P. Minitti, S. Gul, J. Z. Zhang, N. Huse, D. Prendergast, O. Gessner, *J. Phys. Chem. Lett.* **2014**, *5*, 2753.
- [10] C. S. Ponceca, P. Chábera, J. Uhlig, P. Persson, V. Sundström, *Chem. Rev.* **2017**, *117*, 10940.
- [11] M. Gruenewald, L. K. Schirra, P. Winget, M. Kozlik, P. F. Ndione, A. K. Sigdel, J. J. Berry, R. Forker, J.-L. Brédas, T. Fritz, O. L. A. Monti, *J. Phys. Chem. C* **2015**, *119*, 4865.
- [12] C. Bosch-Navarro, B. Matt, G. Izzet, C. Romero-Nieto, K. Dirian, A. Raya, S. I. Molina, A. Proust, D. M. Guldi, C. Marti-Gastaldo, E. Coronado, *Chem. Sci.* **2014**, *5*, 4346.
- [13] P. Schulz, A.-M. Dowgiallo, M. Yang, K. Zhu, J. L. Blackburn, J. J. Berry, *J. Phys. Chem. Lett.* **2016**, *7*, 418.
- [14] I. Robel, B. A. Bunker, P. V. Kamat, *Adv. Mater.* **2005**, *17*, 2458.
- [15] V. O. Koroteev, L. G. Bulusheva, I. P. Asanov, E. V. Shlyakhova, D. V. Vyalikh, A. V. Okotrub, *J. Phys. Chem. C* **2011**, *115*, 21199.
- [16] V. Strauss, A. Roth, M. Sekita, D. M. Guldi, *Chem* **2016**, *1*, 531.
- [17] W.-J. Yin, S.-H. Wei, C. Ban, Z. Wu, M. M. Al-Jassim, Y. Yan, *J. Phys. Chem. Lett.* **2011**, *2*, 2853.
- [18] P. N. O. Gillespie, N. Martsinovich, *J. Phys. Chem. C* **2017**, *121*, 4158.
- [19] A. Erck, W. Sapp, S. Kilina, D. Kilin, *J. Phys. Chem. C* **2016**, *120*, 23197.
- [20] A. Saha, A. Moya, A. Kahnt, D. Iglesias, S. Marchesan, R. Wannemacher, M. Prato, J. J. Vilatela, D. M. Guldi, *Nanoscale* **2017**, *9*, 7911.
- [21] J. E. Weaver, M. R. Dasari, A. Datar, S. Talapatra, P. Kohli, *ACS Nano* **2010**, *4*, 6883.
- [22] S. Kundu, *J. Phys. Chem. C* **2013**, *117*, 23987.
- [23] S. Guo, *Adv. Funct. Mater.* **2013**, *23*, 5199.
- [24] Z. Chen, S. Berciaud, C. Nuckolls, T. F. Heinz, L. E. Brus, *ACS Nano* **2010**, *4*, 2964.
- [25] W.-D. Zhang, L.-C. Jiang, J.-S. Ye, *J. Phys. Chem. C* **2009**, *113*, 16247.
- [26] C. Singh, M. S. P. Shaffer, K. K. K. Koziol, I. A. Kinloch, A. H. Windle, *Chem. Phys. Lett.* **2003**, *372*, 860.
- [27] G. Williams, P. V. Kamat, *Langmuir* **2009**, *25*, 13869.
- [28] F. Vietmeyer, B. Seger, P. V. Kamat, *Adv. Mater.* **2007**, *19*, 2935.
- [29] X. Chen, H. Zhu, Y.-C. Chen, Y. Shang, A. Cao, L. Hu, G. W. Rubloff, *ACS Nano* **2012**, *6*, 7948.
- [30] C. F. Herrmann, F. H. Fabreguette, D. S. Finch, R. Geiss, S. M. George, *Appl. Phys. Lett.* **2005**, *87*, 123110.

- [31] P. Gebhardt, S. W. Pattinson, Z. Ren, D. J. Cooke, J. A. Elliott, D. Eder, *Nanoscale* **2014**, *6*, 7319.
- [32] D. J. Cooke, D. Eder, J. A. Elliott, *J. Phys. Chem. C* **2010**, *114*, 2462.
- [33] N. Kemnade, C. J. Shearer, D. J. Dieterle, A. S. Cherevan, P. Gebhardt, G. Wilde, D. Eder, *Nanoscale* **2015**, *7*, 3028.
- [34] J. M. P. Alaboson, Q. H. Wang, J. D. Emery, A. L. Lipson, M. J. Bedzyk, J. W. Elam, M. J. Pellin, M. C. Hersam, *ACS Nano* **2011**, *5*, 5223.
- [35] C. Singh, M. S. P. Shaffer, A. H. Windle, *Carbon* **2003**, *41*, 359.
- [36] K. Zheng, K. Židek, M. Abdellah, M. Torbjörnsson, P. Chábera, S. Shao, F. Zhang, T. Pullerits, *J. Phys. Chem. A* **2013**, *117*, 5919.
- [37] M. N. Islam, T. B. Ghosh, K. L. Chopra, H. N. Acharya, *Thin Solid Films* **1996**, *280*, 20.
- [38] D. Eder, A. H. Windle, *J. Mater. Chem.* **2008**, *18*, 2036.
- [39] S. Aksel, D. Eder, *J. Mater. Chem.* **2010**, *20*, 9149.
- [40] A. S. Cherevan, P. Gebhardt, C. J. Shearer, M. Matsukawa, K. Domen, D. Eder, *Energy Environ. Sci.* **2014**, *7*, 791.
- [41] Ü. Özgür, Y. I. Alivov, C. Liu, A. Teke, M. A. Reshchikov, S. Doğan, V. Avrutin, S.-J. Cho, H. Morkoç, *J. Appl. Phys.* **2005**, *98*, 041301.
- [42] L. Irimpan, V. P. N. Nampoori, P. Radhakrishnan, A. Deepthy, B. Krishnan, *J. Appl. Phys.* **2007**, *102*, 063524.
- [43] L. Gaudreau, K. J. Tielrooij, G. E. D. K. Prawiroatmodjo, J. Osmond, F. J. G. de Abajo, F. H. L. Koppens, *Nano Lett.* **2013**, *13*, 2030.
- [44] P. Reineck, D. Gómez, S. H. Ng, M. Karg, T. Bell, P. Mulvaney, U. Bach, *ACS Nano* **2013**, *7*, 6636.
- [45] A. Yeltik, G. Kucukayan-Dogu, B. Guzelturk, S. Fardindoost, Y. Kelestemur, H. V. Demir, *J. Phys. Chem. C* **2013**, *117*, 25298.
- [46] C. Bauer, G. Boschloo, E. Mukhtar, A. Hagfeldt, *Chem. Phys. Lett.* **2004**, *387*, 176.
- [47] I. Medintz, N. Hildebrandt, *FRET—Förster Resonance Energy Transfer: From Theory to Applications*, Wiley-VCH, Weinheim, Germany **2014**.
- [48] R. S. Swathi, K. L. Sebastian, *J. Chem. Sci.* **2009**, *121*, 777.
- [49] V. Miikkulainen, M. Leskelä, M. Ritala, R. L. Puurunen, *J. Appl. Phys.* **2013**, *113*, 021301.
- [50] L. Zhang, H. C. Jiang, C. Liu, J. W. Dong, P. Chow, *J. Phys. Appl. Phys.* **2007**, *40*, 3707.
- [51] E. B. Lavik, I. Kosacki, H. L. Tuller, Y. M. Chiang, J. Y. Ying, *J. Electroceram.* **1997**, *1*, 7.
- [52] P. Mondal, A. Klein, W. Jaegermann, H. Hahn, *Solid State Ionics* **1999**, *118*, 331.
- [53] J. Bisquert, *Nanostructured Energy Devices - Equilibrium Concepts and Kinetics*, CRC Press, Boca Raton, FL **2015**.
- [54] P. Liu, Q. Sun, F. Zhu, K. Liu, K. Jiang, L. Liu, Q. Li, S. Fan, *Nano Lett.* **2008**, *8*, 647.
- [55] L. Hu, Y.-L. Zhao, K. Ryu, C. Zhou, J. F. Stoddart, G. Grüner, *Adv. Mater.* **2008**, *20*, 939.
- [56] M. Krissanasaeranee, S. Wongkasemjit, A. K. Cheetham, D. Eder, *Chem. Phys. Lett.* **2010**, *496*, 133.
- [57] A. Janotti, C. G. V. de Walle, *Rep. Prog. Phys.* **2009**, *72*, 126501.
- [58] K. Jacobi, G. Zwicker, A. Gutmann, *Surf. Sci.* **1984**, *141*, 109.